POLITECNICO DI TORINO
Repository ISTITUZIONALE

Aging diagnostics in lithium-ion batteries with differential mechanical measurements

*Original*
Aging diagnostics in lithium-ion batteries with differential mechanical measurements / Clerici, D., Pistorio, F., Soma', A.. - In: APPLIED ENERGY. - ISSN 0306-2619. - ELETTRONICO. - 386:(2025), pp. 1-14. [10.1016/j.apenergy.2025.125524]

*Availability:*
This version is available at: 11583/2997949 since: 2025-02-27T17:51:59Z

*Publisher:*
Elsevier

*Published*
DOI:10.1016/j.apenergy.2025.125524

*Terms of use:*

This article is made available under terms and conditions as specified in the corresponding bibliographic description in the repository

*Publisher copyright*

(Article begins on next page)

16 September 2026

Applied Energy 386 (2025) 125524

Contents lists available at ScienceDirect

Applied Energy

journal homepage: www.elsevier.com/locate/apenergy

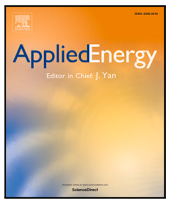

# Aging diagnostics in lithium-ion batteries with differential mechanical measurements

Davide Clerici *, Francesca Pistorio, Aurelio Somà

*Department of mechanical and aerospace engineering, Politecnico di Torino, Corso duca degli Abruzzi, 24, Torino, 10129, Piemonte, Italy*

## GRAPHICAL ABSTRACT

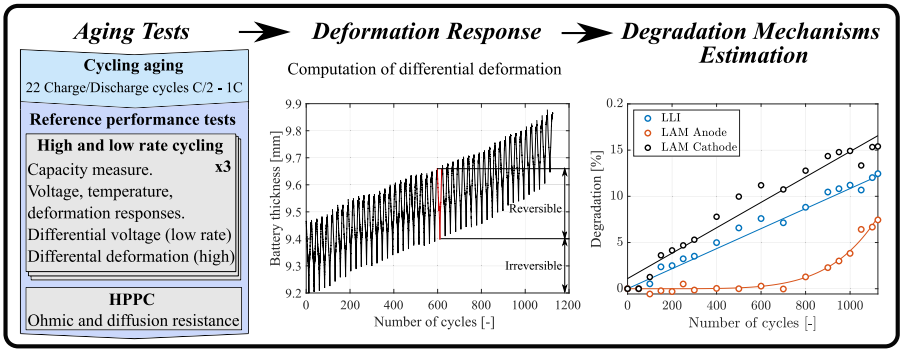


## ARTICLE INFO

Dataset link: https://zenodo.org/records/14914172

*Keywords:*
Lithium-ion batteries
Aging test
LAM and LLI
Irreversible deformation
Degradation mechanisms

## ABSTRACT

This work investigates how the mechanical response of lithium-ion batteries evolves with aging and demonstrates how mechanical measurements can be used to estimate degradation mechanisms, presenting interesting advantages over traditional voltage-based methods. A lithium cobalt oxide-graphite battery was cycled over 1,000 times to a state of health of 70%, with periodic performance tests measuring capacity, resistance, voltage, temperature, and deformation during the charge/discharge cycles. The deformation measurements can be distinguished into a reversible component (expansion during charge recovered with the shrinkage during discharge) and an irreversible component (increase of the battery thickness through aging).

From these measurements, differential deformation and incremental deformation analyses are performed to assess degradation mechanisms, innovatively demonstrating that the loss of active material and the loss of lithium inventory estimated from deformation measurements are perfectly aligned with those estimated with traditional voltage measurements at low current. In contrast to differential voltage, differential deformation offers the significant advantage of being applicable even at high current rates, which are typical of real-world charging profiles.

Finally, the calculated degradation mechanisms are correlated with the physical phenomena occurring within the battery, e.g. the growth of the solid electrolyte interface and particle cracking, finding a satisfactory agreement with the trend of the measured capacity, resistance and reversible, and irreversible deformation.

## 1. Introduction

The limited life of lithium-ion batteries (LIBs) is a significant weakness of this technology and one of the most studied topics in the literature concerning lithium-ion batteries.

The study of battery aging from the experimental point of view is an expensive and time-consuming task. Indeed, even with accelerated tests, several hundreds of charge and discharge cycles are necessary to bring the battery to the end of life (EOL). Furthermore, the aging

* Corresponding author.
*E-mail address:* davide.clerici@polito.it (D. Clerici).

https://doi.org/10.1016/j.apenergy.2025.125524
Received 17 November 2024; Received in revised form 16 January 2025; Accepted 9 February 2025
0306-2619/© 2025 The Authors. Published by Elsevier Ltd. This is an open access article under the CC BY license (http://creativecommons.org/licenses/by/4.0/).

trajectory depends on the charge and discharge rates, depth of discharge (DOD), and temperature [1]. Finally, tests must be repeated on different battery samples under the same condition when the purpose is to develop a predictive model.

Fortunately, several battery aging datasets have been made public over the years, and these have been excellently cataloged and described in a review by Dos Reis et al. [2] dating back to 2021 as well as in a very recent review by Mayemba et al. [3] published in 2024. Furthermore, the repository Battery Archive supported by the U.S. Department of Energy Office of Electricity [4] aims to collect battery aging datasets across different institutions for easy visualization, analysis, and comparison.

Aging datasets can be categorized in constant current cycles (still with different current rates, DOD and temperatures) and drive cycle profiles. Among the constant current aging datasets, it is worth mentioning the one from Nasa [5] (not specified electrode material), Calce [6] (lithium cobalt oxide (LCO)), Sandia [7] (multiple electrode materials), Oxford University [8] (nickel manganese cobalt oxide (NMC)), the European project Everlasting (nickel cobalt aluminum oxide (NCA)) exploring battery aging with different operating current rates and temperatures, Toyota research institute [9–11] (lithium iron phosphate (LFP)) that considered a greater number of batteries but with the same operating condition and the Argonne National Laboratory [12] (LFP). Furthermore, in 2023 a comprehensive battery aging dataset was released by Li et al. from the Iowa State University [13], comprising 225 NMC batteries tested with different charge and discharge currents and DOD. This kind of work was developed to define a statistical model aiming to predict battery life from early aging data [14]. In 2024, another battery aging dataset was released by the Imperial Collage of London [15], studying degradation mechanisms of 40 NMC811-C/SiOx battery cells subjected to different operating conditions (temperature and state of charge (SOC)).

All the datasets previously mentioned reported the capacity, current, voltage, and sometimes the temperature and internal resistance of the tested batteries. Mechanical measurements are included just in the open access aging dataset from Stefanopoulos et al. [16]. Besides this, few other works reported how the mechanical characteristics of the battery change with aging [17–21], and how the external pressure affects the battery performance through life [22,23]. In most of these works, just the irreversible structural expansion of the batteries through aging is documented, generally sensed with a load cell constraining the battery deformation. Other information about the shape of the mechanical deformation curve and its relation with electrical performance are generally not discussed.

Degradation in LIBs comes from the complex interaction between electrochemical and mechanical phenomena [24–26]. Among those, the most significant are the propagation of fracture in the electrode microstructure (particles), triggering or accelerating undesired side reactions such as solid electrolyte interface (SEI) growth, and hindering the movement of lithium-ions or isolating parts of the active material. Pore clogging is another mechanical related phenomenon, possibly correlated with the constrained expansion of the battery during operation, whereas lithium plating is a pure electrochemical phenomenon correlated with fast charging.

Fracture propagation in active material particles is triggered by the so called diffusion-induced stress, resulting from the interaction of lithium ions with the lattice structure of the active material, quantified in relevant works [27–29]. Experimental observation and numerical modelling of fracture propagation in electrodes are discussed extensively in two relevant reviews [30,31], respectively. Fracture can be evaluated from the electrode design characteristics numerically [32,33] or analytically [34,35], then some design guidelines exist to limit fracture and the electrode degradation from the mechanical point of view [36].

The degradation phenomena cited above result in two degradation mechanisms occurring during aging: loss of active material (LAM) and loss of lithium inventory (LLI). Traditionally, these degradation mechanisms are assessed with differential voltage (DV) or incremental capacity (IC) analyses, whose working principle and implementation guidelines are excellently reviewed by Dubarry et al. [37]. Over the years, some software for battery diagnostics based on DV and IC have been developed. Dubarry and al. [38–40] developed the Alawa Toolbox for battery degradation identification employing IC to decode the results of aging test. Dahn et al. [41] developed a similar battery diagnostic tool based on DV analysis. Recently, Chen et al. [42] developed an algorithm implemented in MATLAB to quantify LAM and LLI from DV and IC analysis.

The authors of this work explained the fundamentals of the methodology to decode degradation mechanisms from macroscopic battery deformation measurements in the paper “Diagnostics methodology based on differential mechanical measurements for lithium-ion batteries”. Macroscopic deformation measurements leverage the close correlation between the deformation of the electrode and the concentration of lithium ions, as discussed in [43–45], to identify degradation mechanisms. Furthermore, since the deformation of the electrode is reflected in the overall deformation of the battery, this method allows for the detection of electrode changes through the macroscopic battery deformation [43,46]. This methodology is significantly less affected by the current intensity compared to voltage-based analyses, thus it can also be applied with real-world charging profiles. These interesting properties motivated the authors’ research group to patent a methodology and a device for online charge and health estimation of LIBs based on macroscopic deformation measurements [47].

This work shows the results of a high-cycle (1000+) aging test on a commercial LCO-graphite battery, which reached its end of life at 70% of its state of health (SOH). Besides the traditional voltage response, the mechanical and thermal responses of the battery are innovatively monitored through aging. The aging dataset has been published open-access [48]. The degradation mechanisms are quantified with voltage-based and with an innovative deformation-based methodology developed by the authors and presented in the paper “Diagnostics methodology based on differential mechanical measurements for lithium-ion batteries”. A schematic summary of the main steps of the algorithm is reported in this work as well to ensure the replicability of the results. Finally, the characteristics of the deformation response, such as the reversible and irreversible deformation, are correlated with battery performance decay (capacity loss and resistance rise), explaining for the first time the correlation between mechanical and electrical performances.

In Section 2, the experimental methodology followed to carry out the aging tests is explained. In Section 3.1 the voltage, temperature, and deformation responses change through aging are shown, as well as the electrical (capacity and resistance) and mechanical (reversible and irreversible deformation) performances. Section 3.2 focuses on the differential analyses of the results, studying the differential voltage, differential deformation, incremental voltage, and incremental deformation of the aging dataset. In Section 3.3 the degradation mechanisms (LAM and LLI) are quantified from the differential analyses explained in the previous section. Finally, the performances, responses, and degradation mechanisms identified in the previous sections are discussed in Section 3.4, and correlated with physical degradation phenomena occurring in the battery during aging.

## 2. Experimental methodology

Three commercial LCO-graphite battery samples, whose characteristics are reported in Table 1, are initially characterized as explained in detail in an authors’ prior work [49].

The initial reference performance test (RPT), referring to Fig. 1, consists of: (a) Three complete high current charge–discharge cycles (C/2 constant current (CC)/constant voltage (CV) - 1C CC, respectively); (b) a complete low current charge–discharge cycle (C/20 CC - C/20 CC, respectively); (c) Hybrid pulse power characterization (HPPC) test. One

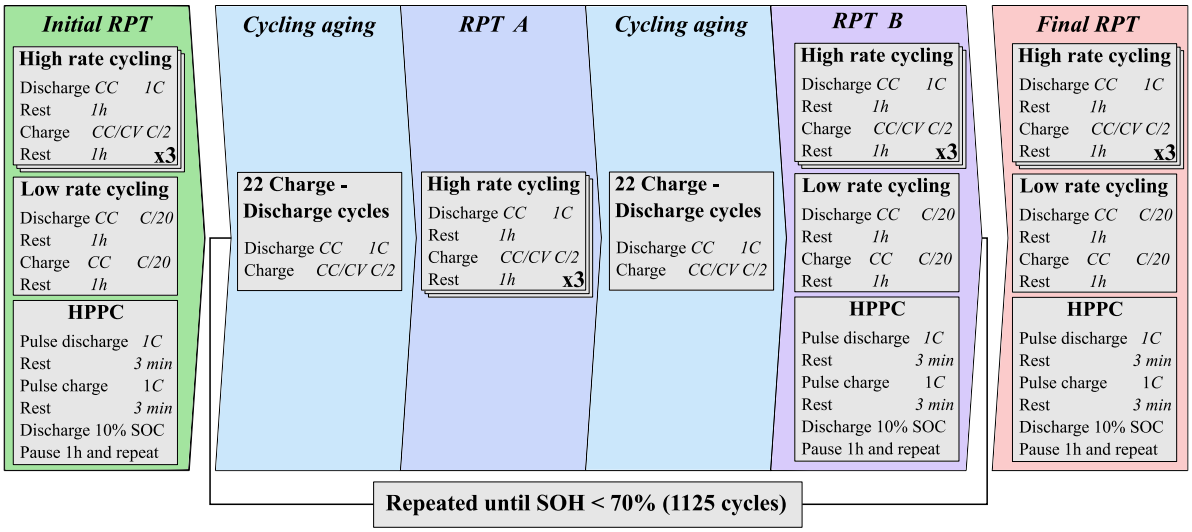


**Fig. 1.** Synthetic description of the aging test protocol.

**Table 1**
LIBs samples properties. The current rate is expressed in C-rate, where 1C is the current needed to completely discharge the battery in one hour.

| | LCO |
|---|---|
| Manufacturer | Melasta |
| Anode | Graphite |
| Cathode | LCO |
| Type | Pouch |
| Length | 182.5 mm |
| Width | 94.5 mm |
| Thickness | 9.2 mm |
| Capacity | 22 Ah |
| Operating voltage | 3 V–4.2 V |
| Max operating current charge | C/2 |
| Max operating current discharge | 5C |
| Thermal expansion coefficient | $2 \cdot 10^{-4}$ °C$^{-1}$ |

hour rest is left between each current profile.

Then, two battery samples are left stored at ambient temperature for calendar aging comparison, and one battery sample undergoes aging test according to the procedure summarized in Fig. 1 and explained below.

The cycling procedure involves aging steps consisting of 22 aging cycles at 1C CC discharge and C/2 CC-CV charge, with no pauses in between. Periodic RPTs are carried out after each aging step. In particular, two series of RPTs are alternated, referred to as RPT-A and RPT-B.

The RPT-A consists of three high rate cycles (1C CC discharge and C/2 CC-CV charge) with 1 h rest. The RPT-B consists of three high rate cycles (1C CC discharge and C/2 CC-CV charge) with 1 h rest, one low rate cycle (C/20) and the HPPC test. In this way, high rate test cycles are carried out periodically every 25 cycles (22 aging + 3 RPT), whereas low rate test cycles and HPPC are carried out every 50 cycles.

High rate test cycles allow measuring the 1C capacity, the voltage, the temperature, and the deformation responses to complete charge/discharge cycles starting from an equilibrium condition. The mean between the three measurements is considered.

Low rate test cycles are necessary to measure the C/20 capacity and the voltage response for differential analysis purposes.

HPPC is used to measure the battery resistance as a function of SOC. In particular, a charge and discharge pulse at 1C is applied for 10 s and 3 min rest is left in between. Then, the battery is discharged CC at 1C for 6 min to move at a 10% lower SOC. 1 h rest is left after discharge and before starting again with the pulse profile. In this way, resistance is measured every 10% SOC from 100% to 10%. Two kinds of resistances are measured: Ohmic resistance and diffusion resistance. Ohmic resistance is measured considering the instantaneous voltage drop after the application of the current at the beginning of the pulse. Diffusion resistance is calculated considering the voltage drop in the 10 s pulse, net of the Ohmic voltage drop. Figure S1 in the supplementary material clarifies the voltage drops considered for the resistance calculation. Ohmic and diffusion voltage drops are divided by the pulse current to calculate Ohmic and diffusion resistance. The testing procedure previously described is chosen to speed up the aging test while maintaining good accuracy in tracking the degradation path of the battery. 1125 charge–discharge cycles were achieved before reaching the SOH 70% and stopping the test. A final RPT equal to RPT-B was carried out at the end of life.

The purpose of this study is to demonstrate the effectiveness of mechanical-based methods in estimating the degradation mechanisms of single batteries subjected to aging. The focus is not on characterizing the aging behaviour of a specific battery type. Therefore, only a single battery was aged in this study, and a statistical analysis of the aging behaviour across multiple samples is considered not meaningful for the purposes of this study. It is remarked that if the proposed estimation algorithm was applied to multiple batteries, different results would have been obtained for each sample just because each battery follows its own aging trajectory. This does not affect the robustness of the proposed method, as demonstrated by the consistency of its results with those of state-of-the-art methodologies, such as differential voltage analysis.

The battery test bench consists of a power supply “QPX600DP” by Aim-TTi, an electronic load “EL 9080-400” by Elektro-Automatik, a thermistor mounted on the battery surface, and a couple of laser sensors “optoNCDT 1900-10LL” by MicroEpsilon for measuring the battery thickness change. The National Instruments controller “NI PXIe-8840” is used for the real-time control. The tests are carried out at a constant temperature equal to 20° in a thermostatic chamber by MSL.

The laser sensors are mounted on a dedicated structure, ensuring perpendicularity between the laser beam and the battery surface and keeping the battery fixed during the acquisition process, according to Fig. 2. Thickness change measurements are carried out sensing the out-of-plane displacement of the central point of the two larger surfaces of the battery sample, as shown in Fig. 2b–c. The authors reported in a previous work additional details on the test bench and the procedure to characterize the battery samples [49].

The aging dataset is available open access in the Zeonodo repository [48].

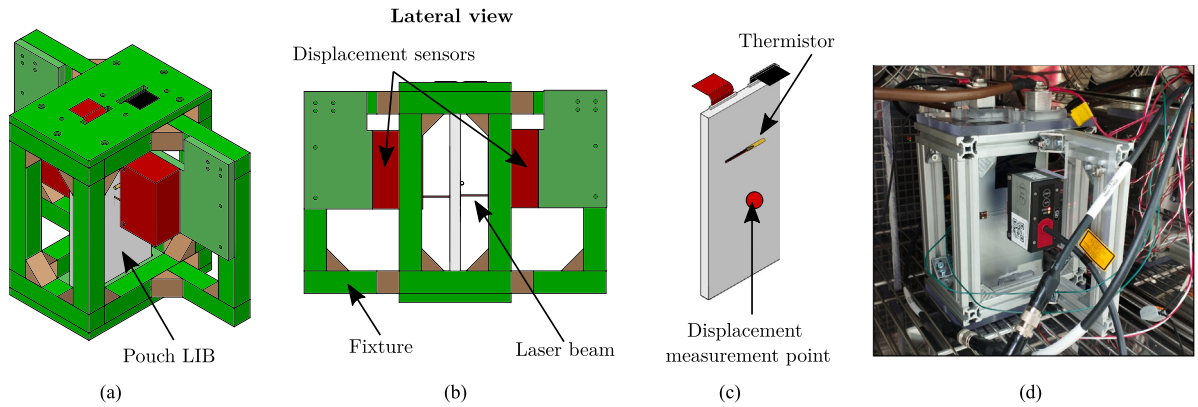


**Fig. 2.** Experimental set-up for the macroscopic deformation (thickness change) measurements of pouch LCO-Gr battery samples. (**a–c**) Schematic of the measurement set-up, (**d**) picture of the measurement set-up.

## 3. Results and discussion

In this section, the results of the aging test are provided and discussed. First, the changes in the battery performance and response are addressed. Secondly, these results are leveraged to identify the degradation mechanisms and further explain the degradation path of the tested battery as well as the correlation with physical degradation phenomena.

### 3.1. Response and performance change through battery life

The changes in battery voltage, deformation and temperature responses through aging are shown in Fig. 3.

Concerning the voltage response, the first evident result is the continuous decrease of the voltage level during discharge (or increase during charge) through aging, as observed in Fig. 3a,d, revealing an increase in the internal resistance. The progressive voltage decrease during discharge is slightly greater than the progressive increase during charge due to the higher current used during discharge, which, given the same resistance, results in a larger voltage drop. Furthermore, a significantly greater voltage drop is observed during both charge and discharge in the final RPT, attributed to the sharp increase in resistance at the end of life.

The shape of the deformation response does not change significantly through aging, except for the obvious shrinking along the horizontal axis because of the capacity loss (Fig. 3b,e). Nevertheless, its shape remains almost unchanged if plotted as a function of SOC (Fig. 3f). The only significant difference occurs at the last RPT, characterized by a significant lower capacity, thus lower deformation. Actually, also the curves from the 800th cycle onwards show a slight progressive contraction in the maximum deformation value.

The temperature change slightly increases through aging because of the increase in resistance, as observed in Fig. 3c. The peak in the temperature change during discharge is caused by the entropic heat of LCO: its entropic coefficient has a marked peak at about y = 0.6 [50], corresponding to the beginning of the discharge of the full battery, roughly at 2.5 Ah. This results in a temperature peak of the entire battery, because of the significant entropic contribution given by LCO to the heat generated (and absorbed when the temperature goes down after the peak) by the entire battery. The peak progressively cancels after 800 cycles because the increasing resistance makes the Ohmic heat predominant on the entropic heat. Such greater heat release overcomes the heat entropically absorbed by the LCO which causes the temperature drop between 3 Ah and 5 Ah before the 800 cycles. Temperature during charge is not reported because of the modest variation observed.

The capacity loss, the Ohmic and diffusion resistance raise are quantified in Fig. 4. The 1C capacity in Fig. 4a, shows a marked knee point at approximately 800 cycles. Subsequently, an instantaneous drop is observed at 1125 cycles, where more than 2% capacity was lost each cycle, quickly reaching SOH 70%. On the other hand, the C/20 capacity follows the same trend of the 1C capacity until 800 cycles, and then it keeps the same trend until the end of life. The different behaviour between the 1C and C/20 capacity is supposed to be caused by a progressive increase in resistance after 800 cycles, which leads to a faster decrease in the 1C capacity because the voltage cut-off is reached earliest due to the higher voltage drop.

This hypothesis is quite in agreement with internal resistance measurements obtained with HPPC tests and reported in Fig. 4b–c. Indeed, both the Ohmic and diffusion resistances increase almost linearly after the 400th cycle, followed by a faster increase in the last RPTs. The Ohmic resistance is supposed to be caused by the partial disconnection of the current collector from the electrode layer, possibly because of cracks, copper dissolution, and aluminium corrosion. Binder decomposition within the electrode layer can be the cause of Ohmic resistance increase as well [51]. Diffusion resistance is assumed to be caused mainly by the growth of the SEI layer, as well as the propagation of cracks in the active material particles, that increase the tortuosity hindering the passage of lithium ions. Pore clogging has the same effect causing the increase of tortuosity and diffusion resistance [51].

These observations and the discrepancy between the 1C and C/20 capacity suggest the existence of at least two different degradation mechanisms: one causing the capacity fade baseline identified by the C/20 capacity curve (red circles in Fig. 4a); another causing the significant resistance increase after 800 cycles and the consequent faster capacity loss observed in the 1C capacity curve (blue crosses in Fig. 4a).

Concerning the mechanical performance of the battery through aging, Fig. 5a shows the mechanical response recorded during the high rate cycling RPTs. The mechanical response can be divided into two contributions: (a) The reversible deformation, namely the expansion and contraction during charge and discharge, respectively; (b) The irreversible deformation, namely the slight and continuous expansion of the battery thickness through aging. Reversible and irreversible deformation are plotted separately in Fig. 5a–b, respectively. The reversible deformation measured during high rate cycling (blue crosses in Fig. 5a) keeps constant at 0.25 mm until 800 cycles, except for the first slight ripple between 0.255 mm and 0.245 mm, whose cause is unknown. Then, a steep linear decrease is observed after 800 cycles. On the other hand, the reversible deformation measured during the low rate cycling (red circles in Fig. 5a) keeps quite constant at about 0.265 mm, with some noise. The higher reversible deformation is justified by the wider stoichiometric window resulting from the lower lithium inhomogeneity

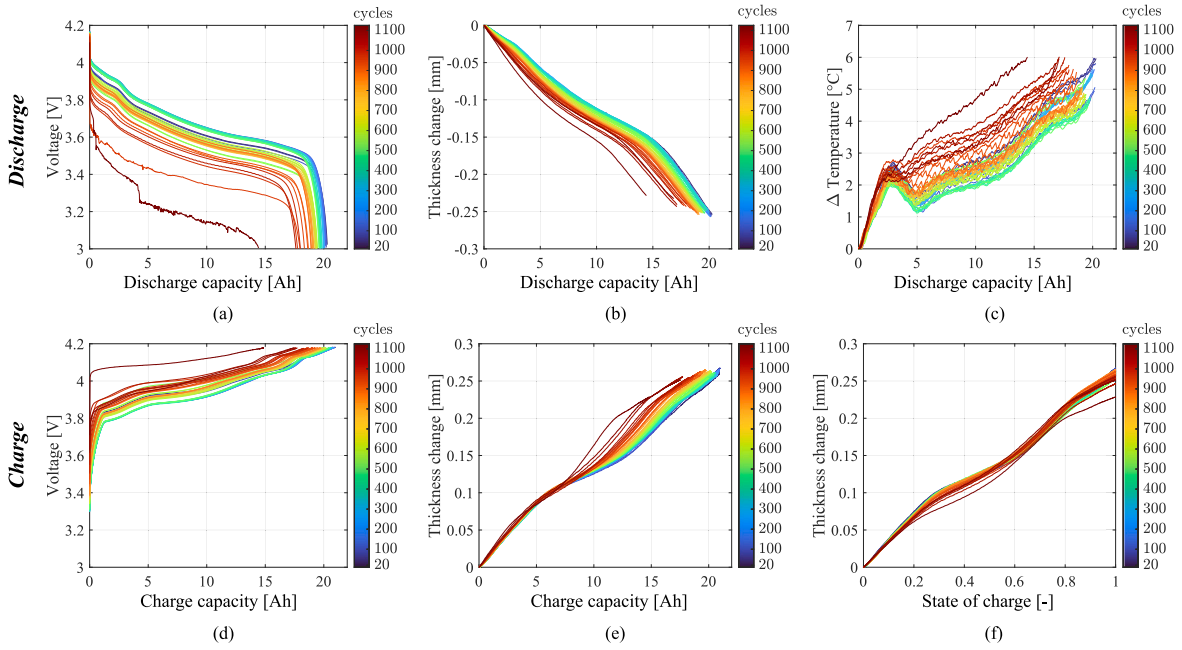


**Fig. 3.** Battery responses change measured during the high rate RPTs through aging. (**a**) Voltage, (**b**) deformation and (**c**) temperature responses to 1C discharge. (**d**) Voltage and (**e**) deformation responses to C/2 charge. (**f**) Deformation response to C/2 charge as a function of state of charge.

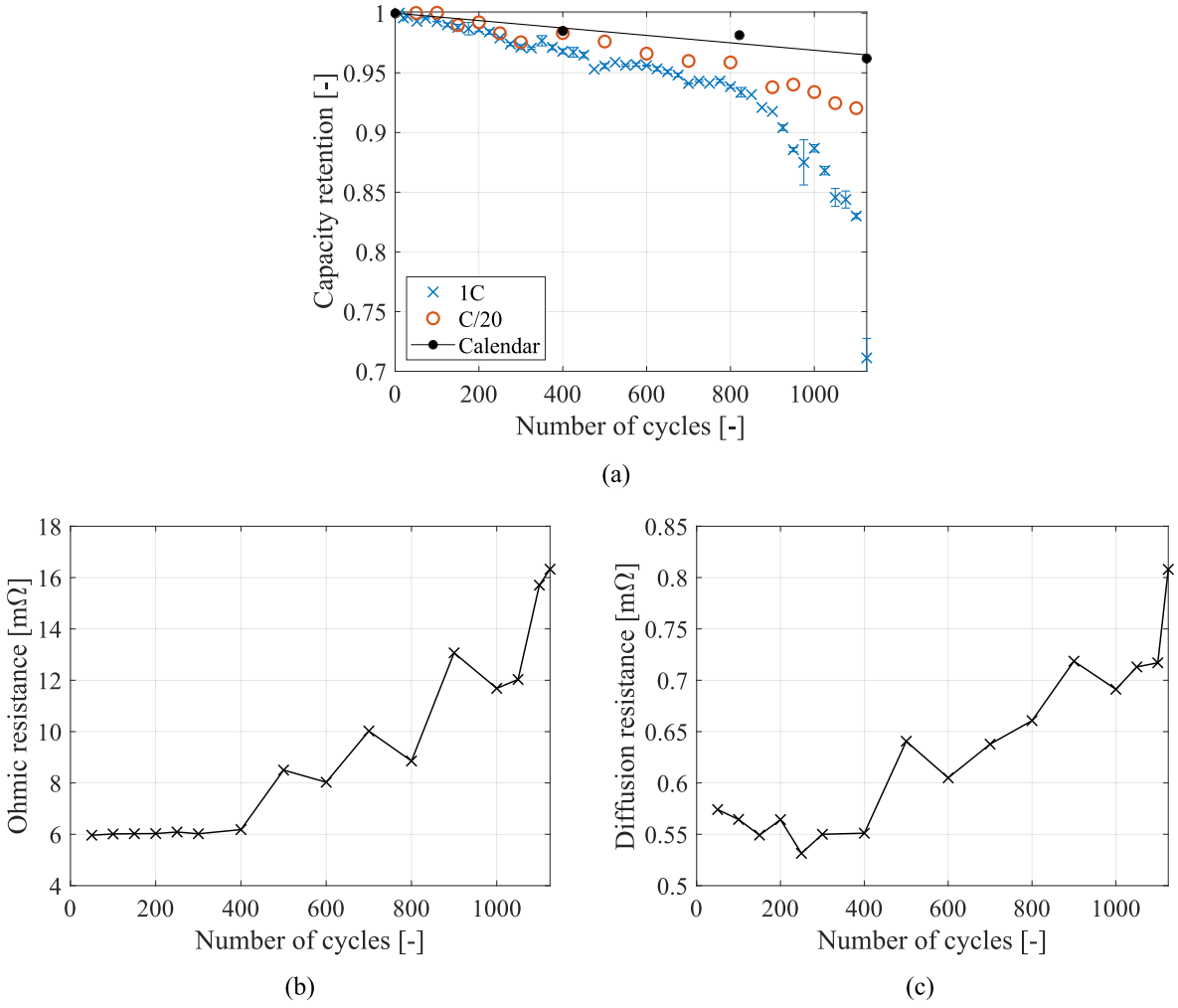


**Fig. 4.** Electrical performance changes through aging. (**a**) C/20, 1C capacities and the reference calendar, (**b**) Ohmic resistance and (**c**) Diffusion resistance. Error bars refer to the standard deviation of the measurements repeated three times in each single RPT, and the symbol refers to the mean value.

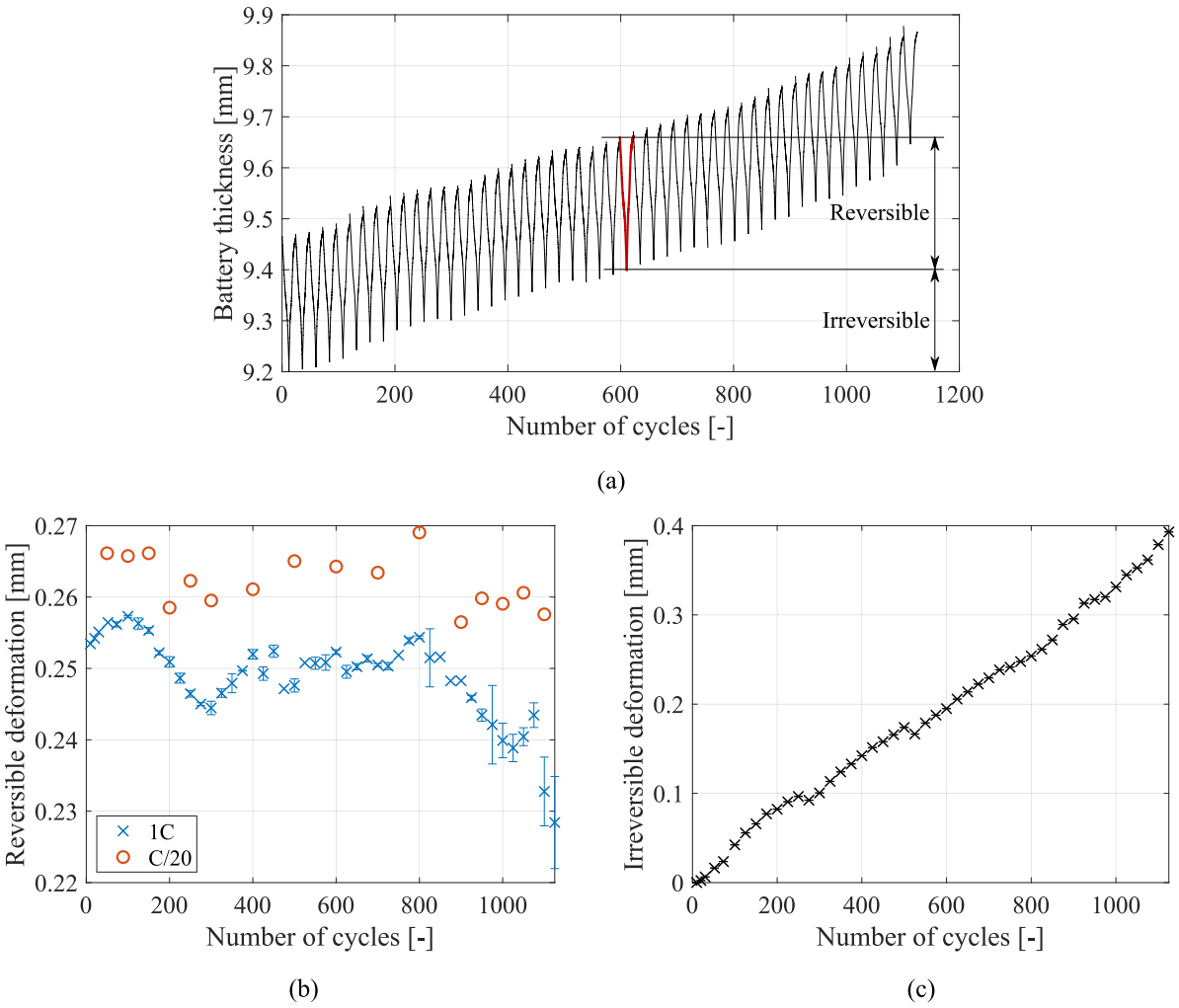


**Fig. 5.** Mechanical performances changes through aging. (**a**) Battery thickness change recorded during high rate cycling RPTs. (**b**) Reversible deformation and (**c**) irreversible deformation. Error bars refer to the standard deviation of the measurements repeated three times in each single RPT, and the symbol refers to the mean value.

in the electrode and its particles achieved at a lower cycling rate, leading to a higher electrode deformation as will be deepened in Section 3.4.3.

Furthermore, the reversible deformation measured during 1C and C/20 RPTs perfectly matches the 1C and C/20 capacity measurements reported in Fig. 4a: when the capacity loss follows the baseline, reversible deformation remains the same, in fact it remains constant during the whole life with C/20 cycling RPT and until 800 cycles with 1C cycling RPT. Then, the faster capacity loss from 800 cycles measured with 1C cycling RPTs and the resistance rise perfectly matches the contraction of the reversible deformation observed after the same number of cycles. The reason behind this behaviour will be deepened in Section 3.4.3.

The irreversible deformation, reported in Fig. 5b, shows a perfect linear trend through the whole battery life and appears to be closely correlated to the capacity baseline of the battery measured with the C/20 capacity test.

A further explanation of the physical phenomena causing the correlation between electrical and mechanical performances will be given in Section 3.4, identifying and discussing the degradation mechanisms leading to the performance decay observed in Figs. 4–5.

### 3.2. Differential measurements

Differential voltage (DV) and differential expansion (DE) are calculated from the voltage and deformation measurements in a charge or discharge cycle as reported in Eqs. (1a)–(1b), respectively.

$$DV = \frac{dV}{dQ} \tag{1a}$$

$$DE = \frac{d^2(thk)}{dQ^2} \tag{1b}$$

where $thk$ is the battery thickness, correlated with the deformation (thickness change).

Differential voltage is calculated as the derivative of the voltage ($V$) with respect to the capacity ($Q$) of the battery. On the other hand, differential expansion is calculated as the second derivative of the deformation curve (reported in Fig. 3b,e) with respect to the capacity.

The second derivative of the deformation is computed instead of the first derivative because this curve shows peaks and valleys corresponding to the peaks and valleys of the differential voltage curve. Indeed, phase transitions cause plateaus in the voltage curve, so the start and the end of the transition can be detected by peaks in the first derivative of the curve. On the other hand, phase transitions cause changes in the slope of the deformation curve, which appear as peaks when computing the second derivative. The correspondence between deformation and voltage features is extensively discussed in the authors' paper "Diagnostics methodology based on differential mechanical measurements for lithium-ion batteries". Briefly, the features of both curves highlight phase transitions occurring at a precise lithium concentration in the electrode, causing marked voltage and deformation changes, resulting in peaks in the corresponding differential

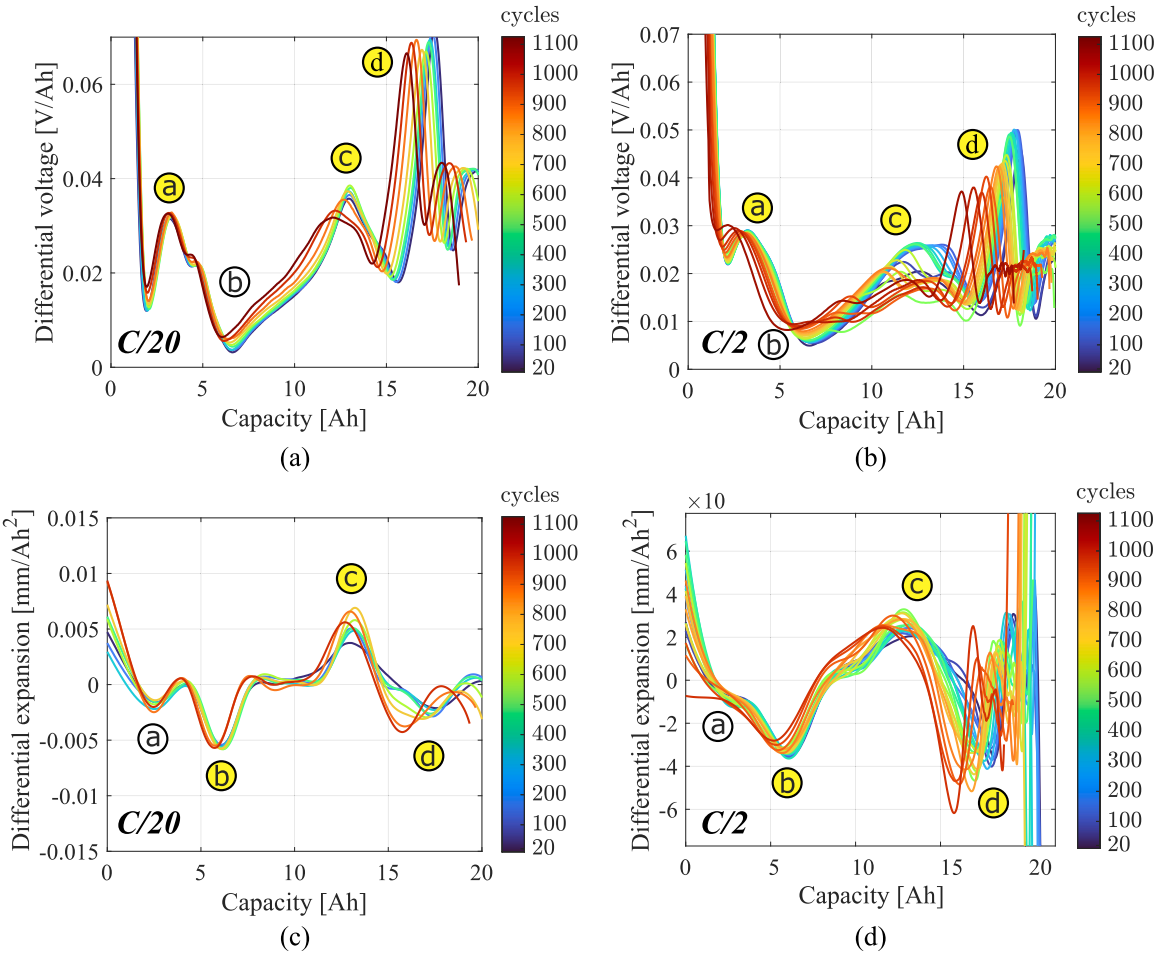


**Fig. 6.** Differential measurements through aging. (**a–b**) Differential voltage recorded during low and high rate charge RPTs. (**c–d**) Differential expansion recorded during low and high rate charge RPTs. The peaks labelled with the highlighted letters are used to calculate the working conditions of the electrodes (capacity and stoichiometric indexes) and thus the degradation indicators (LAM and LLI).

voltage and differential expansion curves. As these features identify a precise lithium concentration in the electrode, and thus SOC, they can be used to track the degradation mechanisms going on in the battery, following the methodology explained in Section 3.3.

Differential voltage and differential expansion during charge are plotted in Fig. 6a–b and c–d, computed from the RPTs carried out at C/20 and C/2, respectively. The peaks marked in the curves identify the boundaries of two stage transitions and one solid solution of graphite and the boundaries of two stage transitions of LCO. Most importantly, differential analyses in Fig. 6 capture how the occurrence of phase transition changes with aging.

In particular, the peak labelled *a* of the DV curve corresponds to the coexistence between stages IIIL and IVL of graphite ("L" stands for liquid, i.e. absence of visible lithium-ions ordering). The peaks labelled *b* and *c* represent the beginning and the end of the phase transition from stage IIIL to stage II of graphite, respectively. Then, the valley *b* corresponds to pure stage IIIL and the peak *c* corresponds to pure stage II. Furthermore, the peak *b* is superimposed to the beginning of the phase transition of LCO from hexagonal II to hexagonal I phase. Finally, the peak labelled *d* corresponds to the pure monoclinic phase of LCO. Just the peaks highlighted in yellow are used to compute the electrode working conditions (capacities and stoichiometric indexes) and thus the degradation indicators (LAM and LLI), as just two features for each electrode are needed for the electrode identification, as detailed in Section 3.3.

The problem with the DV analysis is that such features become difficult to identify at higher currents, typical of real-world applications, because the voltage polarization and the electrode inhomogeneity cause the flattening and the broadening of the peaks [52], as evidenced by comparing Fig. 6a–b. In particular, peak *c* in Fig. 6b becomes very flat and its position is impossible to be identified. Furthermore, also peak *a* almost disappears already at C/2 (observe how peak *a* lowers increasing the current comparing Fig. 6a and 6b). On the other hand, the differential expansion curve shows the same features attributable to graphite and LCO transitions as the DV, but such features remain observable even at high current rate, as demonstrated by the correspondence of the peaks in Fig. 6c–d. Indeed, the positions of the peaks *b*, *c* and *d* in Fig. 6d are clearly identifiable and they can be used to track degradation at high current as done traditionally with DV.

The same reasoning holds also for the incremental analyses. Incremental capacity (IC) and incremental expansion (IE) can be computed from the voltage and deformation measurements according to Eqs. (2a)–(2b) and are reported in Fig. 7a–b and c–d for C/20 and C/2 charge, respectively. Incremental capacity tells the amount of charge exchanged per unit of Volt, whereas incremental expansion tells the amount of deformation occurring per unit of Volt.

$$IC = \frac{dQ}{dV} \tag{2a}$$

$$IE = \frac{d(thk)}{dV} \tag{2b}$$

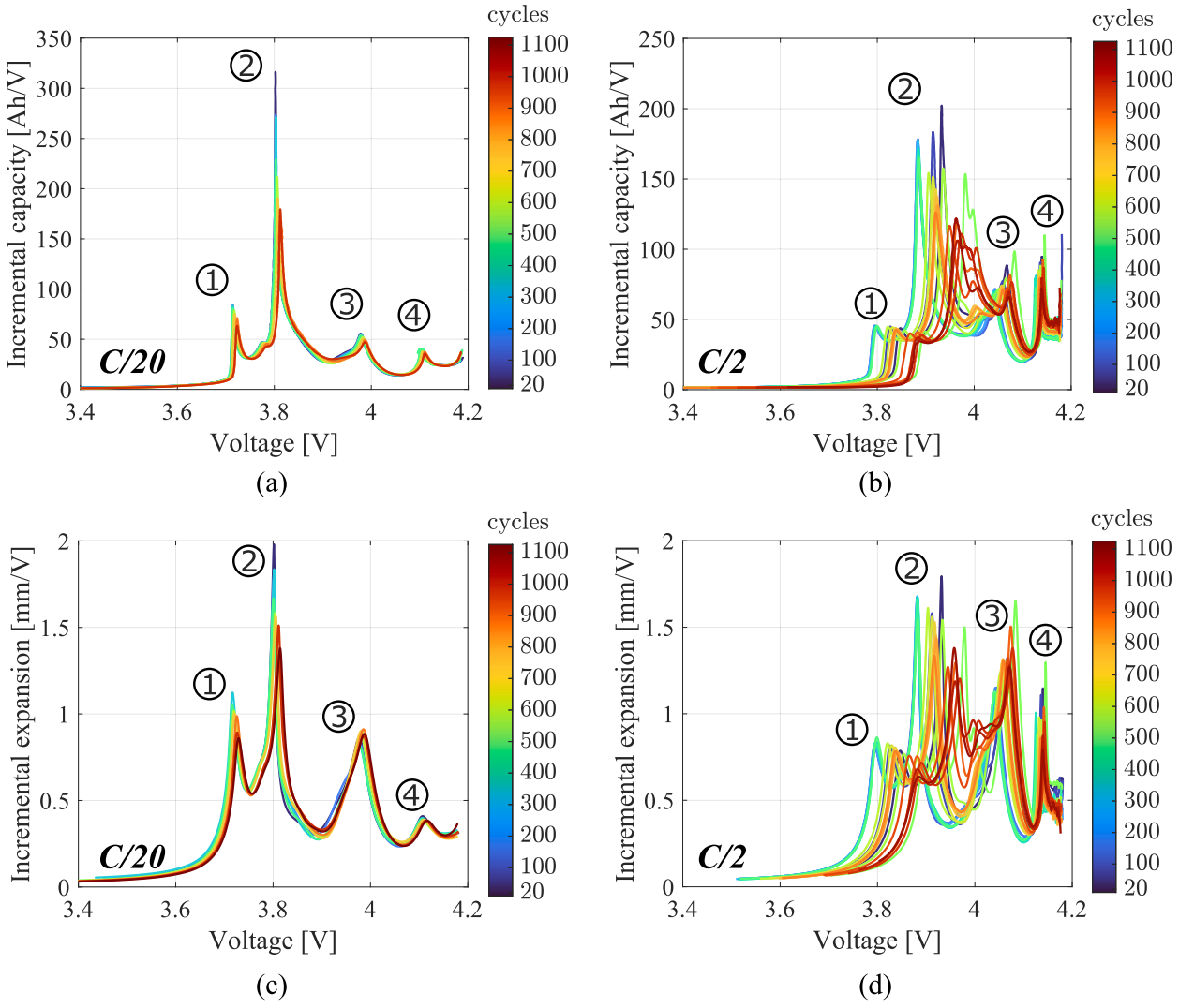


**Fig. 7.** Incremental measurements through aging. (**a–b**) Incremental voltage recorded during low and high rate charge RPTs. (**c–d**) Incremental expansion recorded during low and high rate charge RPTs.

As evidenced previously for the differential curves, the features (peaks) in the incremental curves can be attributed to phase transitions occurring in the electrode at precise voltage (and SOC) values. Furthermore, an exact correlation between the features in the IC and IE curves is evidenced in Fig. 7. The features in the curves correspond to the same reactions described for the differential analyses with one important distinction: the peak in the differential curves tells the boundary (beginning or end) of a phase transition, and so the occurrence of a pure phase (solid solution). On the other hand, the peaks in the incremental curves tell the occurrence of a phase transition.

Then, the peak labelled 1 corresponds to the stage transition 1L-IVL of graphite. The peak labelled 2 corresponds to the stage transition IIIL-II of graphite, superimposed to the phase transition of LCO between the two hexagonal phases I and II. The peak labelled 3 corresponds to the transition between phases hexagonal II and monoclinic of LCO. Finally, the peak labelled 4 corresponds to the transition between the monoclinic and hexagonal phase of LCO.

Incremental curves are not used to quantitatively compute the working conditions of the electrodes (capacity and stoichiometric indexes), but they can qualitatively reveal the degradation mechanisms (LAM and LLI) occurring in the battery by studying how the peaks of the curve change in amplitude and shift along the voltage axis.

The loss of active material is identified by the reduction in amplitude of the peaks in the IC and IE curves. Indeed, the IC curve tells the amount of capacity exchanged at a certain voltage. Similarly, the IE curve tells the amount of deformation occurring at a certain voltage, and deformation is dependent on capacity: the greater the capacity exchanged by the battery, the greater the swelling of the battery, as can be observed in Fig. 3e–f and demonstrated in authors' previous work [43,46,49]. This means that if the peaks in IC and IE lower, the electrode causing those peaks is losing capacity. Thus, it is possible to qualitatively describe the LAM of the negative and positive electrode from the change in the peak amplitude of the IC and IE curves, reported in Figure S2 of the supplementary material and described in the following lines.

Peak 1 is uniquely caused by graphite, and its change in amplitude through aging is exponential. Peak 2 has a linear amplitude decrease, and it is given by the contribution both of graphite and LCO because both the electrodes show a phase transition at 3.8 V (battery voltage). Therefore, one may assume that the dominant electrode is the one with the phase transition spanning a longer capacity, thus causing a higher peak in the IC/IE curve. Nevertheless, the electrode with faster capacity reduction causes a major change in the peak amplitude. Hence, a qualitative estimation is not reliable in case of superimposed peaks of two electrodes. Peak 3 is correlated with a phase transition of LCO and shows a linear reduction in amplitude. Peak 4 is also due to LCO, its amplitude exhibits a linear downward trend at the beginning of cycling but accelerates towards the last cycles. In the end, it is

observed that peaks correlated with graphite exhibit an exponential amplitude decrease, whereas peaks correlated with LCO exhibit a linear amplitude decrease through aging. This observation is confirmed by the computation of the capacity of the negative and positive electrodes in Section 3.3, which shows that the LAM for the negative and positive electrodes follows an exponential and a linear trend, respectively.

The loss of lithium inventory is definitely more challenging to observe from IC and IE. LLI causes a change in the stoichiometric indexes of the electrodes, which could cause a change in the voltage at which the phase transitions occur. At the same time, the shift in voltage of the occurrence of phase transitions could be caused by the resistance increase through aging. This effect is dominant in the aging dataset of this work, as the voltage shift of the peaks in the IC/IE curves, reported in Figure S3 of the supplementary material, shows the same trend of the resistance change reported in Fig. 4b–c. Therefore, the voltage shift of the peaks in IC/IE reveals as a valuable tool to quantify the battery resistance change.

### 3.3. Calculation of degradation mechanisms

The degradation mechanisms occurring in the battery subjected to aging test are numerically quantified in this section from the voltage and deformation measurements. At first, the change through aging of the electrodes capacities and the working stoichiometric indexes are computed from differential analysis. Afterward, the loss of active material and the loss of lithium inventory are quantified from electrodes capacities and stoichiometric limits. This methodology has been deepened in the authors' paper "Diagnostics methodology based on differential mechanical measurements for lithium-ion batteries". Hence, the steps of the algorithm are just briefly summarized below and graphically outlined in Figure S4 of the supplementary material to ensure the replicability of the results.

1. The voltage, the thickness change, and the capacity of the full battery are measured (Fig. 3) in a charge or discharge cycle.
2. After filtering the data, DV and DE are computed according to Eq. (1) ($DV = \frac{dV}{dQ}$ and $DE = \frac{d^2(thk)}{dQ^2}$). Filtering is the crucial step of the method, because the numerical computation of the derivatives amplifies the noise of the measurements. The Golay-Savitzky filter showed good performance for this purpose.
3. Peaks of DV or DE of the full battery are identified and associated with the specific peaks of the differential potential and second derivative of the crystal strain of the single electrodes, reported in Figure S4. The peaks positions of the negative electrode are indicated as $Q_n^j$ (DV/DE of the full battery) and $x^j$ (DV/DE of the single electrode). On the other hand, the peaks positions of the positive electrode are indicated as $Q_p^k$ (DV/DE of the full battery) and $y^k$ (DV/DE of the single electrode), where $j$ and $k$ identify the peaks of the negative and positive electrode, respectively.
4. Two matched pairs of peaks are chosen for each electrode, namely $(Q_n^1, x^1)$ and $(Q_n^2, x^2)$ for the negative electrode (peaks $a$ and $c$ in DV and peaks $b$ and $c$ in the DE, referring to Fig. 6), and $(Q_p^1, y^1)$ and $(Q_p^2, y^2)$ for the positive electrode (peaks $c$ and $d$ in DV and DE, referring to Fig. 6).
5. The capacities of the negative and positive electrode ($C_n$ and $C_p$) are computed according to Eqs. (3a)–(3b), and they are plotted in Fig. 8a–b. Once the capacity of the electrodes is known, the stoichiometric limits of the negative and positive electrodes are computed using Eq. (4), and they are plotted in Fig. 8c–d.

$$C_n = \frac{\Delta Q_n}{\Delta x} = \frac{Q_n^2 - Q_n^1}{x^2 - x^1} \tag{3a}$$

$$C_p = \frac{\Delta Q_p}{\Delta y} = \frac{Q_p^2 - Q_p^1}{y^2 - y^1} \tag{3b}$$

$$x_{100} = x^1 + \frac{Q_n^1}{C_n} \tag{4a}$$

$$x_0 = x_{100} - \frac{Q_{full}}{C_n} \tag{4b}$$

$$y_{100} = y^1 - \frac{Q_p^1}{C_p} \tag{4c}$$

$$y_0 = y_{100} + \frac{Q_{full}}{C_p} \tag{4d}$$

6. LLI is defined as the loss of lithium inventory with respect to the fresh state, according to Eq. (5).

$$LLI = \frac{n_{Li}^{fresh} - n_{Li}^{aged}}{n_{li}^{fresh}} = 1 - \frac{x_{100}^{aged} C_n^{aged} + y_{100}^{aged} C_p^{aged}}{x_{100}^{fresh} C_n^{fresh} + y_{100}^{fresh} C_p^{fresh}} \tag{5}$$

where $n_{Li}$ is the total lithium content in the electrodes, $n_{Li} = \frac{3600}{F}(x_z C_n + y_z C_p)$.
7. LAM expresses the reduction of the capacity of the negative and positive electrode, and it is computed according to Eqs. (6a)–(6b), respectively.

$$LAM_n = 1 - \frac{C_n^{aged}}{C_n^{fresh}} \tag{6a}$$

$$LAM_p = 1 - \frac{C_p^{aged}}{C_p^{fresh}} \tag{6b}$$

The capacity of the negative electrode is reported in Fig. 8a and shows an exponential decrease, whereas the capacity of the positive electrode is reported in Fig. 8b and shows a more consistent linear decrease. These results are identical both when calculated at high rate with DE and low rate with DV, as demonstrated later with the calculation of the LAM.

The trends of the stoichiometric limits calculated from the low rate DV are reported in Fig. 8c–d for the positive and negative electrodes, respectively. The width of the stoichiometric window of the negative and positive electrode is calculated from the stoichiometric limits as $x_{100} - x_0$ and $y_0 - y_{100}$, respectively. The width of the stoichiometric window of negative and positive electrode calculated both from the low-rate DV and the high rate DE is reported in Fig. 8e–f.

Two facts are pointed out: (a) the stoichiometric window is wider when cycling at a lower rate, because of the lower lithium inhomogeneity in the electrode and in its particles, resulting in a more efficient electrode utilization; (b) the stoichiometric window at high rate exponentially decreases after 800 cycles (especially in the negative electrode) as a consequence of the resistance increase and the early reaching of the voltage limits, as will be discussed in Section 3.4.3.

Then, the loss of active material and loss of lithium inventory are computed with Eqs. (5)–(6) from the electrode capacities and stoichiometric limits as a function of the number of cycles. Such degradation mechanisms as a function of the number of cycles are reported in Fig. 9, computed from the voltage measurements at low current.

To prove the capabilities of the differential deformation analysis, the estimation of the degradation mechanisms from the DV at low current and the DE at high current are compared in Fig. 10. Since the degradation indicators (LAM and LLI) represent the battery's state and should remain consistent regardless of the current rate used in testing, Fig. 10 demonstrates that the estimation obtained through differential expansion–applicable to both low and high current charge/discharge cycles–aligns perfectly with the estimation from the traditional voltage-based method, which is only valid at extremely low currents. Indeed, at high current rates, the DV analysis is not feasible due to the loss of curve features caused by voltage polarization and electrode inhomogeneity. This result also highlights the advantage of

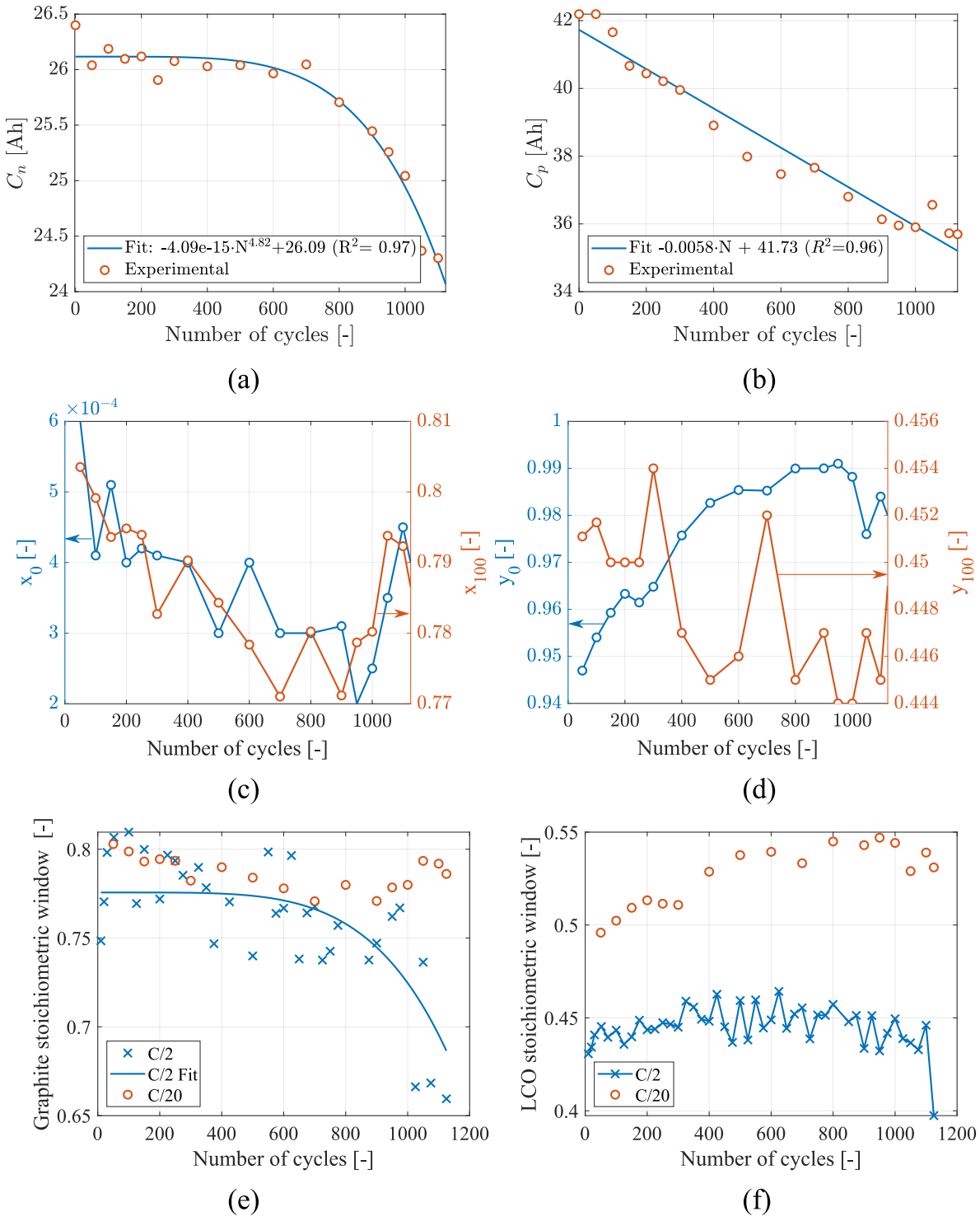


**Fig. 8.** Change of electrode working conditions through aging computed from DV analysis at low current, where not specified differently. (**a**) Capacity of the negative electrode, (**b**) capacity of the positive electrode, (**c**) stoichiometric indexes of the negative electrode at soc 0% and 100%, (**d**) stoichiometric indexes of the positive negative electrode at soc 0% and 100%, (**e–f**) Width of the stoichiometric window of the negative and positive electrodes at low (with DV) and high rate (with DE).

the proposed deformation-based method, which can diagnose the battery performance at high current, as required in real-world applications, overcoming the limitations of traditional voltage-based methods that can only be used in laboratory settings with very low current.

Furthermore, the agreement of degradation indicators computed with two different methodologies (the traditional differential voltage and proposed differential expansion), performed on different datasets – Differential voltage is performed on the reference performance test carried out at low current (C/20), whereas differential expansion is performed on the reference performance test carried at high current (C/2) - guarantees the reliability of the results.

The main drawback to report is the scattering of the estimation at high current (especially in the LAM of the negative electrode), also due to the higher number of measurements available at the higher rate.

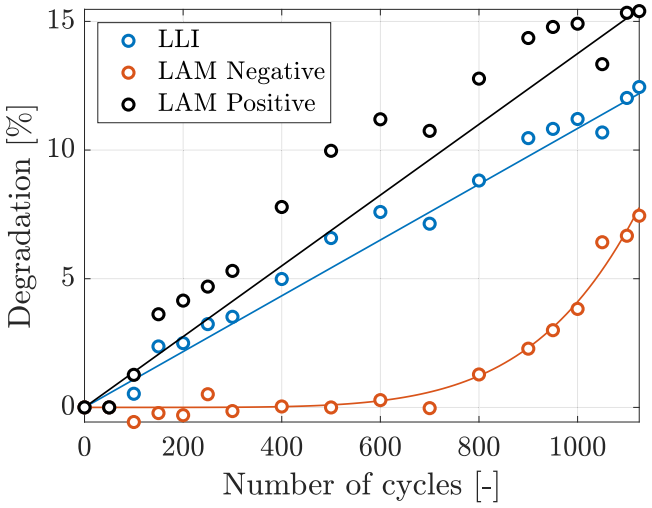


**Fig. 9.** Degradation mechanisms through aging computed from DV analysis at low current. LLI and LAM positive are linearly fitted, whereas LAM negative is fitted with a power law as a function of the number of cycles (N) according to the following expressions: LLI = 0.0108 N; LAM negative = $2.3\,10^{-16}$ $N^{5.4}$; LAM positive = 0.0137 N.

Nevertheless, the fit of the estimation is well in agreement with the DV at low current. The scattering in some of the DE estimations, especially those related to negative electrode properties, is caused by two reasons: (a) DE is calculated by deriving two times the measured thickness change during operation. The numerical computation of derivatives amplifies the noise of the measurement and advanced filtering strategies must be adopted to control this problem. This is the only very weak point of the DE methodology. (b) Lithium concentration inhomogeneity through the electrode (but not within the particles) affects at a lower extent also the deformation measurements, broadening the peaks in the DE and making it difficult to identify their exact position, especially peak *c* in Fig. 6d related to graphite.

### *3.4. Interpretation of the correlation between electrical and mechanical responses and the degradation mechanisms*

In this section, an in-depth interpretation of the results is given, correlating the measured battery responses and performances with the calculated degradation mechanisms and the physical degradation phenomena at the root of them.

#### *3.4.1. LLI and irreversible deformation*

LLI shows a perfect linear trend according to Fig. 9. Assuming that the loss of lithium is mainly caused by side reactions such as the SEI growth, this result is in agreement with the SEI growth law under kinetic-limited condition, which is linear with time [31]. This result is also in agreement with the observed irreversible deformation (Fig. 5c) and partially with the trend of the diffusion resistance (Fig. 4c), as well as the linear capacity fade at C/20, which is likely to be caused by the growth of the SEI layer.

For what concerns irreversible deformation, generally it may be assumed to be caused by the SEI growth reaction and lithium plating [53]. Lithium plating is considered scarcely influential in this aging dataset because of the absence of fast charging. On the other hand, in the SEI growth reaction, the gas formed in the reaction is assumed to be responsible for the irreversible deformation, rather than the solid SEI compound. Hence, assuming that all the irreversible deformation is caused by the SEI growth reaction, the linear trend of the irreversible deformation is perfectly in agreement with the linear trend of LLI, which in turn is the result of the growth of the SEI layer.

The SEI layer covering active material particles, besides consuming lithium ions, it also hinders the passage of the ions during (de) intercalation in the particle, causing the progressive increase of the so called diffusion resistance as a function of the SEI thickness, thus the number of cycles [51]. Hence, it is supposed that also the diffusion resistance grows linearly as the SEI layer. Actually, the diffusion resistance keeps almost constant until 400 cycles, and then a linear increase is observed afterwards (refer to Fig. 4c).

#### *3.4.2. Loss of active material and mechanical damage of electrodes*

The loss of active material of the positive and negative electrodes follows the same trend of the electrode capacities (Fig. 8a–b). Then, the loss of material in the positive electrode has a linear trend and it is significantly larger than the loss of material in the negative electrode, having an exponential trend quickly increasing after 800 cycles. The higher LAM of the positive electrode is supposed to be correlated with the more critical fracture behaviour of LCO with respect to graphite. The fracture toughness of LCO is lower than graphite [31], being 0.94 MPa$\sqrt{m}$ [54] versus 1.42 MPa$\sqrt{m}$ [55], thus LCO is more prone to fracture. This consideration is also supported from the experimental point of view, as LCO is much more prone to fracture because of the peculiar phase transitions [30].

The exponential trend of the loss of active material of the negative electrode is in agreement with the knee point of the capacity curve at the battery level. Indeed, the knee point in the capacity curve is supposed to be primarily caused by the steep resistance increase after 800 cycles, and resistance increase is generally attributed to loss of active material, because fracture and material fragmentation hinder the diffusion of lithium ions, in agreement with Edge et al. [25]. Dubarry et al. [40] observed that LAM commonly follows a power-law or exponential dependence, as also supported by experimental evidences [56,57].

In the literature, the physics-based models predicting the battery life rely on the physical description of the degradation mechanisms going on inside the battery. In particular, the loss of active material is considered to be caused by the fracture propagation and the mechanical degradation of the electrode microstructure [24,25]. Then, LAM is traditionally modelled with a damaging law dependent on the stress in the particle as reported in Eq. (7a). The expression of LAM as a function of the number of cycles is got in Eq. (7b) integrating Eq. (7a).

$$\frac{dLAM}{dN} = K\Delta\sigma^m \tag{7a}$$

$$LAM = K\Delta\sigma^m N \tag{7b}$$

Eq. (7b) shows that the approach usually adopted in literature is able to model just a linear LAM, which is not what observed experimentally in this work, as well as in other experimental works in the literature [56,57].

Starting from this consideration, the authors propose an expression for modelling the loss of active material that considers both the dependence on the stress (directly related to the current delivered by the battery), both the non-linear correlation with the number of cycles, as observed experimentally in this work. In this case, Eq. (7) modifies in Eq. (8).

$$\frac{dLAM}{dN} = K\Delta\sigma^m N^n \tag{8a}$$

$$LAM = \frac{K}{n+1}\Delta\sigma^m N^{n+1} = a\Delta\sigma^m N^b \tag{8b}$$

where $a = \frac{K}{n+1}$, and $b = n + 1$. Eq. (8) can clearly describe also the linear LAM, setting the coefficient $n$ to zero and coming back to Eq. (7). Eq. (8b) fits perfectly the non linear LAM of the negative electrode reported in Fig. 9b, with $a = 2.33\,10^{-16}$ and $b = 5.41$, as well as the linear LAM of the positive electrode with $a = 0.0137$ and $b = 1$. Aging was carried out at a single current rate, then the dependence on the stress cannot be investigated experimentally in this work, and the term $\Delta\sigma^m$ is set to 1 to compute the parameters $a$ and $b$. Even though, it is observed in literature that higher current leads to higher LAM [58], proving the correctness of the term $\Delta\sigma^m$ in Eq. (8).

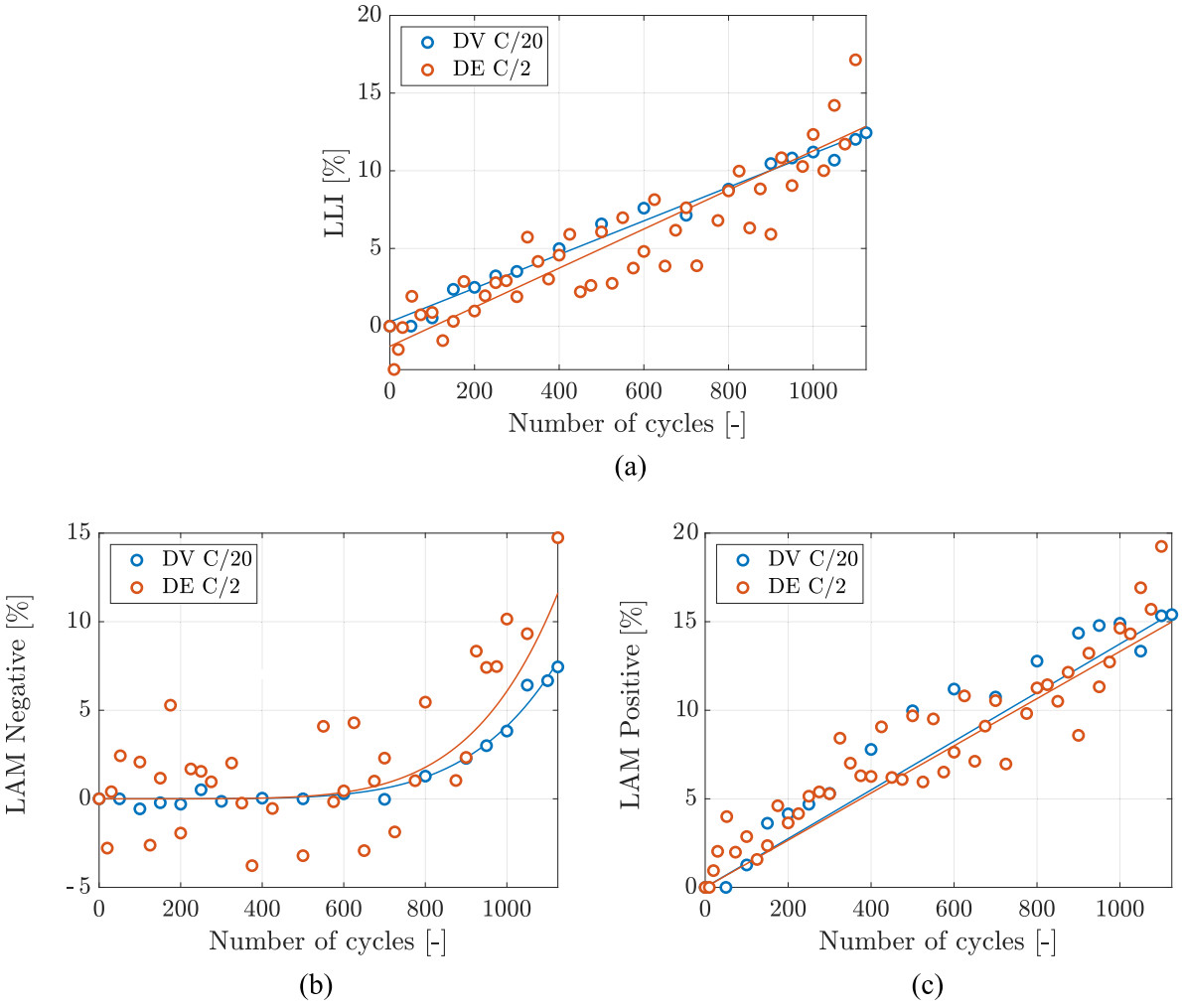


**Fig. 10.** Comparison of degradation mechanisms computed from DV analysis at low current and DE analysis at high rate. (**a**) LLI, (**b**) LAM negative, (**c**) LAM positive. LLI and LAM positive are linearly fitted, whereas LAM negative is fitted with a power law as a function of the number of cycles (N) according to the following expressions: LLI = 0.0108 N + 0.3 (C/20), 0.0126 N − 1.3 (C/2); LAM negative = $2.3\,10^{-16}$ $N^{5.4}$ (C/20), $1.9\,10^{-16}$ $N^{5.5}$ (C/2); LAM positive = 0.0137 N (C/20), 0.0133 N (C/2).

### 3.4.3. Correlation between capacity and reversible deformation

Concerning the capacity retention shown in Fig. 4a, the low rate and high rate capacities have a similar trend until 800 cycles. After that, the high rate capacity shows a knee point and decreases much faster than the low rate capacity, that keeps the same linear trend.

The battery capacity is the combination of the electrode capacity and the width of the stoichiometric window according to Eq. (9), plotted in the supplementary material in Figure S6, quite in agreement with the measured capacity retention at high and low rate shown in Fig. 4a.

$$Q = C_n(x_{100} - x_0) = C_p(y_0 - y_{100}) \tag{9}$$

The change in the electrode capacity is quantified by the LAM (Fig. 10b–c), whereas the change in the stoichiometric window is reported in Fig. 8e–f. As the LAM is the same for high and low current, the discrepancy between the high and low rate capacity is caused by the significant shrinkage of the working stoichiometric window after 800 cycles when cycling at high current. This, in turn, is due to the increased internal resistance observed in Fig. 4b–c, which causes the voltage limits to be reached earlier, thereby reducing electrode utilization. Resistance rise after 800 cycles is possibly caused by the exponential increase of the LAM in the negative electrode after 800 cycles. Indeed, LAM is caused by fracture propagation, increasing the tortuosity and hindering the passage of lithium ions, and it is generally considered the responsible for the steep resistance increase and the consequent knee point in the capacity curve [25,58].

On the other hand, the low rate capacity is unaffected by such resistance-related degradation mechanism and keeps the same linear trend for the whole battery life connected with the SEI growth.

The reversible deformation is closely correlated to the battery capacity, thus the electrode capacity (LAM) and the width of the stoichiometric window. The deformation of the battery during operation is expressed in Eq. (10), as described in an authors' previous work [43].

$$\Delta t_{rev} = K_{case} N_{lay} \left( (\varepsilon_n^c(x_{100}) - \varepsilon_n^c(x_0))\zeta_n t_n + (\varepsilon_p^c(y_{100}) - \varepsilon_p^c(y_0))\zeta_p t_p \right) + \alpha t_{nom} \Delta T \tag{10}$$

where $\alpha t_{nom} \Delta T$ is the thermal contribution that can be neglected for this purpose because it has a low influence [49] and the temperature change is modest, $K_{case}$ is the stiffness of the external case (for prismatic batteries), $N_{lay}$ is the number of electrode layers, $\varepsilon_n^c$ and $\varepsilon_p^c$ are the crystal strain of the negative and positive electrode (Figure S5a–b), $\zeta_n$ and $\zeta_p$ are the active material fraction in the negative and positive electrodes, and $t_n$ and $t_p$ are their thicknesses.

The reversible deformation reported in Fig. 5b gives two information: when cycling a low rate, the reversible deformation keeps the same for the whole battery life, and it is slightly higher than the reversible deformation obtained when cycling at high rate, which is constant until 800 cycles and then shows a knee point and quickly decreases towards the end of life. This trend is perfectly in agreement

with the low rate and high rate battery capacities reported in Fig. 4b and discussed before. Indeed, battery capacities and the amount of reversible deformation are directly proportional, as can be deduced joining Eqs. (9) and (10) and in-depth discussed in authors' previous works [43,46,49].

It turns out that the reversible deformation described by Eq. (10) depends both on the stoichiometric limits (the larger the stoichiometric window of the electrode, the larger its deformation, because the crystal strain of the electrode is monotone), both on the active material fraction, thus the LAM. Indeed, the loss of active material results in a reduction of the deformation-active material in the electrode.

It is important to point out that the crystal strain of the graphite is much larger than LCO, being 13% [59,60] versus 2% [60], according to Figure S5a–b in the Supplementary material. Then, considering the electrode thicknesses and active material fractions of positive and negative electrodes in the same order of magnitude, the deformation of the battery is likely to be dominated by the deformation of the negative electrode (graphite).

Furthermore, the change in the negative active material fraction (LAM negative) is negligible with respect to the change in graphite strain ($\varepsilon^c_{t,n}(x_{100}) - \varepsilon^c_{t,n}(x_0)$ plotted in Figure S5c–d), caused by the contraction of the stoichiometric window during aging. It results that the reversible deformation contracts at higher rate after 800 cycles because of the shrinkage of the stoichiometric window of the negative electrode, that is due to the early reaching of the voltage limits during operation because of the increasing resistance. Furthermore, the reversible deformation achieved at low rate before the knee at 800 cycles is always slightly higher than the reversible deformation at high rate because of the wider stoichiometric window at low rate due to the more efficient electrode utilization and lower lithium concentration inhomogeneity, both in the electrode and in its particles.

## 4. Conclusions

This work shades the light on the in-operando deformation of lithium-ion batteries during aging and proposes the innovative method called – differential expansion – based on deformation measurements as an effective tool to estimate degradation mechanisms, offering advantages over traditional differential and incremental voltage analyses. To demonstrate the capability of this diagnostic method, a commercial LCO/graphite battery was cycled over 1000 times to reach 70% SOH, with periodic performance tests measuring capacity, resistance, as well as the voltage, temperature, and deformation responses to charge/discharge cycles at high and low current.

Differential and incremental expansion analyses were performed, showing that these methods provide the same insights into electrodes' phase transitions as traditional voltage-based methods at low currents. The results demonstrate that deformation-based methods allow the estimation of degradation mechanisms at high currents (1C), typical of automotive charging rates enabling reliable diagnostics in industrial environment, with results consistent with those obtained from voltage-based methods at low currents (C/20) carried out in the laboratory.

The second key contribution of this work is the explanation of the relationship between the estimated degradation mechanisms and the physical degradation processes within the battery. The observed linear loss of lithium inventory aligns with SEI growth and corresponds to the measured linear irreversible deformation. Additionally, the different rates of active material loss in the two electrodes are supposed to be related to the different fracture mechanics behaviour, with LCO being more prone to fracture than graphite, resulting in higher material loss. Finally, a quantitative correlation is demonstrated between battery capacity and reversible deformation at both low and high rates.

## CRediT authorship contribution statement

**Davide Clerici:** Writing – review & editing, Writing – original draft, Visualization, Validation, Methodology, Investigation, Formal analysis, Data curation, Conceptualization. **Francesca Pistorio:** Writing – review & editing, Software, Methodology, Formal analysis, Conceptualization. **Aurelio Somà:** Writing – review & editing, Supervision, Resources, Project administration, Funding acquisition, Formal analysis.

## Declaration of competing interest

The authors declare that they have no known competing financial interests or personal relationships that could have appeared to influence the work reported in this paper.

## Appendix A. Supplementary data

Supplementary material related to this article can be found online at https://doi.org/10.1016/j.apenergy.2025.125524.

## Data availability

The data have been made available open access on zenodo (https://zenodo.org/records/14914172).

## References

[1] Li T, Zhou Z, Thelen A, Howey DA, Hu C. Predicting battery lifetime under varying usage conditions from early aging data. Cell Rep Phys Sci 2024;5.
[2] Dos Reis G, Strange C, Yadav M, Li S. Lithium-ion battery data and where to find it. Energy AI 2021;5:100081.
[3] Mayemba Q, Mingant R, Li A, Ducret G, Venet P. Aging datasets of commercial lithium-ion batteries: A review. J Energy Storage 2024;83:110560.
[4] U D of Energy Office of Electricity. Battery archive. 2020, https://batteryarchive.org/index.html.
[5] Nasa. Nasa prognostics data repository. 2009, https://www.nasa.gov/intelligent-systems-division/discovery-and-systems-health/pcoe/pcoe-data-set-repository/.
[6] Calce. Calce battery data. 2011, https://calce.umd.edu/battery-data.
[7] S N Laboratories. Sandia battery data. 2020, https://www.batteryarchive.org/snl_study.html.
[8] Howey D. Oxford battery intelligence lab - data and code. 2020, https://howey.eng.ox.ac.uk/data-and-code/.
[9] Attia, Severson. Calce battery data. 2020, https://data.matr.io/1/.
[10] Attia PM, Grover A, Jin N, Severson KA, Markov TM, Liao Y-H, Chen MH, Cheong B, Perkins N, Yang Z, et al. Closed-loop optimization of fast-charging protocols for batteries with machine learning. Nature 2020;578:397–402.
[11] Severson KA, Attia PM, Jin N, Perkins N, Jiang B, Yang Z, Chen MH, Aykol M, Herring PK, Fraggedakis D, et al. Data-driven prediction of battery cycle life before capacity degradation. Nat Energy 2019;4:383–91.
[12] Paulson NH, Kubal J, Ward L, Saxena S, Lu W, Babinec SJ. Feature engineering for machine learning enabled early prediction of battery lifetime. J Power Sources 2022;527:231127.
[13] Li T. Isu-ilccnmc/gr battery aging dataset. 2023, https://iastate.figshare.com/articles/dataset/_b_ISU-ILCC_Battery_Aging_Dataset_b_/22582234.
[14] Li T, Zhou Z, Thelen A, Howey D, Hu C. Predicting battery lifetime under varying usage conditions from early aging data. 2023, arXiv preprint arXiv:2307.08382.
[15] Kirkaldy N, Samieian MA, Offer GJ, Marinescu M, Patel Y. Lithium-ion battery degradation: Comprehensive cycle ageing data and analysis for commercial 21700 cells. J Power Sources 2024;603:234185.
[16] Mohtat P, Lee S, Siegel JB, Stefanopoulou AG. Reversible and irreversible expansion of lithium-ion batteries under a wide range of stress factors. J Electrochem Soc 2021;168:100520.
[17] Willenberg LK, Dechent P, Fuchs G, Sauer DU, Figgemeier E. High-precision monitoring of volume change of commercial lithium-ion batteries by using strain gauges. Sustainability 2020;12:557.
[18] Estevez MAP, Conte FV, Tremonti C, Renzi M. Aging estimation of lithium ion cells under real-world conditions through mechanical stress measurements. J Energy Storage 2023;64:107186.
[19] Li R, Ren D, Guo D, Xu C, Fan X, Hou Z, Lu L, Feng X, Han X, Ouyang M. Volume deformation of large-format lithium ion batteries under different degradation paths. J Electrochem Soc 2019;166:A4106.
[20] Louli A, Ellis L, Dahn J. Operando pressure measurements reveal solid electrolyte interphase growth to rank li-ion cell performance. Joule 2019;3:745–61.

[21] Cannarella J, Arnold CB. State of health and charge measurements in lithium-ion batteries using mechanical stress. J Power Sources 2014;269:7–14.

[22] von Kessel O, Avdyli A, Vrankovic D, Birke KP. Swelling, pressure evolution and aging in high-silicon/graphite composite lithium-ion batteries. J Power Sources 2024;610:234582.

[23] Li R, Li W, Singh A, Ren D, Hou Z, Ouyang M. Effect of external pressure and internal stress on battery performance and lifespan. Energy Storage Mater 2022;52:395–429.

[24] Birkl CR, Roberts MR, McTurk E, Bruce PG, Howey DA. Degradation diagnostics for lithium ion cells. J Power Sources 2017;341:373–86.

[25] Edge JS, O'Kane S, Prosser R, Kirkaldy ND, Patel AN, Hales A, Ghosh A, Ai W, Chen J, Yang J, et al. Lithium ion battery degradation: what you need to know. Phys Chem Chem Phys 2021;23:8200–21.

[26] Mocera F, Soma A, Clerici D. Study of aging mechanisms in lithium-ion batteries for working vehicle applications. In: 2020 15th international conference on ecological vehicles and renewable energies. EVER 2020, 2020, http://dx.doi.org/10.1109/EVER48776.2020.9243079.

[27] Clerici D, Mocera F, Somà A. Analytical solution for coupled diffusion induced stress model for lithium-ion battery. Energies 2020;13. http://dx.doi.org/10.3390/en13071717.

[28] Clerici D, Mocera F, Somà A. Shape influence of active material microstructure on diffusion and contact stress in lithium-ion batteries. Energies 2020;14:134. http://dx.doi.org/10.3390/en14010134, URL: https://www.mdpi.com/1996-1073/14/1/134.

[29] Clerici D, Mocera F. Micro-scale modeling of Lithium-ion battery. IOP Conf Ser: Mater Sci Eng 2021;1038:012007. http://dx.doi.org/10.1088/1757-899x/1038/1/012007.

[30] Pistorio F, Clerici D, Mocera F, Somà A. Review on the experimental characterization of fracture in active material for lithium-ion batteries. Energies 2022;15:9168.

[31] Pistorio F, Clerici D, Mocera F, Soma A. Review on the numerical modeling of fracture in active materials for lithium ion batteries. J Power Sources 2023;566:232875.

[32] Pistorio F, Clerici D, Mocera F, Somà A. Coupled electrochemical–mechanical model for fracture analysis in active materials of lithium ion batteries. J Power Sources 2023;580:233378.

[33] Clerici D, Mocera F, Pistorio F. Analysis of fracture behaviour in active materials for lithium ion batteries. In: IOP conference series: materials science and engineering, vol. 1214, IOP Publishing; 2022, 012018.

[34] Pistorio F, Clerici D, Somà A. Analytical computation of stress intensity factor for active material particles of lithium ion batteries. Eng Fract Mech 2023;292:109597.

[35] Pistorio F, Clerici D. Analytical computation of stress intensity factor for multi-physics problems. In: IOP conference series: materials science and engineering, vol. 1306, IOP Publishing; 2024, 012009.

[36] Clerici D, Pistorio F, Somà A. Design and fracture mechanics of lithium-ion batteries. Procedia Struct Integr 2024;58:23–9.

[37] Dubarry M, Anseán D. Best practices for incremental capacity analysis. Front Energy Res 2022;10:1023555.

[38] Dubarry M, Svoboda V, Hwu R, Liaw BY. Incremental capacity analysis and close-to-equilibrium ocv measurements to quantify capacity fade in commercial rechargeable lithium batteries. Electrochem Solid-State Lett 2006;9:A454.

[39] Dubarry M, Liaw BY, Chen M-S, Chyan S-S, Han K-C, Sie W-T, Wu S-H. Identifying battery aging mechanisms in large format li ion cells. J Power Sources 2011;196:3420–5.

[40] Dubarry M, Truchot C, Liaw BY. Synthesize battery degradation modes via a diagnostic and prognostic model. J Power Sources 2012;219:204–16.

[41] Dahn HM, Smith A, Burns J, Stevens D, Dahn J. User-friendly differential voltage analysis freeware for the analysis of degradation mechanisms in li-ion batteries. J Electrochem Soc 2012;159:A1405.

[42] Chen J, Marlow MN, Jiang Q, Wu B. Peak-tracking method to quantify degradation modes in lithium-ion batteries via differential voltage and incremental capacity. J Energy Storage 2022;45:103669.

[43] Clerici D, Mocera F, Soma A. Electrochemical–mechanical multi-scale model and validation with thickness change measurements in prismatic lithium-ion batteries. J Power Sources 2022;542:231735.

[44] Clerici D, Pistorio F, Mocera F, Somà A. Mechanical characterization and modelling of lithium-ion batteries. Transp Res Procedia 2023;70:276–83.

[45] Clerici D, et al. Mechanics of lithium-ion batteries-a modelling and experimental perspective. 2024.

[46] Clerici D, Mocera F. Experimental characterization of lithium-ion cell strain using laser sensors. Energies 2021.

[47] Aurelio Somà FM. Device and method to measure and estimation of state of charge and state of health of a battery. 2022, WO2022269538A1.

[48] Clerici D, Pistorio F, Somà A. Aging dataset LCO battery with mechanical measurements, http://dx.doi.org/10.5281/zenodo.14914172.

[49] Clerici D, Martelli S, Mocera F, Somà A. Mechanical characterization of lithium-ion batteries with different chemistries and formats. J Energy Storage 2024;84:110899.

[50] Thomas KE, Newman J. Heats of mixing and of entropy in porous insertion electrodes. J Power Sources 2003;119:844–9.

[51] Pastor-Fernández C, Widanage WD, Marco J, Gama-Valdez M-A, Chouchelamane GH. Identification and quantification of ageing mechanisms in lithium-ion batteries using the eis technique. In: 2016 IEEE transportation electrification conference and expo. ITEC, IEEE; 2016, p. 1–6.

[52] Bloom I, Christophersen J, Gering K. Differential voltage analyses of high-power lithium-ion cells: 2. applications. J Power Sources 2005;139:304–13.

[53] Weng A, Olide E, Kovalchuk I, Siegel JB, Stefanopoulou A. Modeling battery formation: Boosted sei growth, multi-species reactions, and irreversible expansion. J Electrochem Soc 2023;170:090523.

[54] Swallow JG, Woodford WH, McGrogan FP, Ferralis N, Chiang Y-M, Van Vliet KJ. Effect of electrochemical charging on elastoplastic properties and fracture toughness of lixcoo2. J Electrochem Soc 2014;161:F3084.

[55] Sun G, Bhattacharya S, Alpas A. Cyclic strain-induced crack growth in graphite during electrochemical testing in propylene carbonate-based li-ion battery electrolytes. J Mater Sci 2018;53:1297–309.

[56] Dubarry M, Truchot C, Liaw BY, Gering K, Sazhin S, Jamison D, Michelbacher C. Evaluation of commercial lithium-ion cells based on composite positive electrode for plug-in hybrid electric vehicle applications. part ii. degradation mechanism under 2 c cycle aging. J Power Sources 2011;196:10336–43.

[57] Seo G, Ha J, Kim M, Park J, Lee J, Park E, Bong S, Lee K, Kwon SJ, Moon S-p, et al. Rapid determination of lithium-ion battery degradation: High c-rate lam and calculated limiting lli. J Energy Chem 2022;67:663–71.

[58] Attia PM, Bills A, Planella FB, Dechent P, Dos Reis G, Dubarry M, Gasper P, Gilchrist R, Greenbank S, Howey D, et al. "Knees" in lithium-ion battery aging trajectories. J Electrochem Soc 2022;169:060517.

[59] Didier C, Pang WK, Guo Z, Schmid S, Peterson VK. Phase evolution and intermittent disorder in electrochemically lithiated graphite determined using in operando neutron diffraction. Chem Mater 2020;32:2518–31. http://dx.doi.org/10.1021/acs.chemmater.9b05145.

[60] Koerver R, Zhang W, de Biasi L, Schweidler S, Kondrakov AO, Kolling S, Brezesinski T, Hartmann P, Zeier WG, Janek J. Chemo-mechanical expansion of lithium electrode materials–on the route to mechanically optimized all-solid-state batteries. Energy Environ Sci 2018;11:2142–58.